IX International Conference on Computational Methods for Coupled Problems in Science and Engineering
COUPLED PROBLEMS 2021
E. Oñate, M. Papadrakakis and B. Schrefler (Eds)

VARIATIONAL COMPUTATIONAL MODELLING OF DYNAMICAL BEHAVIOUR OF FIBER ROVING COMPOSITES WITH INELASTIC ANISOTROPIC CONTINUA AND THERMOMECHANICAL COUPLING

MICHAEL GROSS*, JULIAN DIETZSCH†, INIYAN KALAIMANI‡ AND TALHA SALEH♭

Technische Universität Chemnitz
Professorship of Applied Mechanics and Dynamics
webpage: https://www.tu-chemnitz.de/mb/TMD
email: * michael.gross@mb.tu-chemnitz.de,
† julian.dietzsch@mb.tu-chemnitz.de,
‡ iniyan.kalaimani@mb.tu-chemnitz.de,
♭ tmd@mb.tu-chemnitz.de

Key words: Fiber-reinforced material, anisotropic thermo-viscoelasticity, mixed finite element method, higher-order energy-momentum scheme, mixed principle of virtual power.

Abstract. The nonlinear finite element method is a computational method in the variational simulation of material models for materials with and without microstructures [1]. Taking into account microstructures of engineering materials in their computational models is often worthwhile to improve numerical predictions [2]. An example is the modelling of fiber-reinforced materials, which are manufactured on the microscale by filaments or on the mesoscale by rovings, respectively. A macroscopic finite element simulation of both materials provides an anisotropic continuum model. However, fiber-reinforced materials based on rovings demand for continua with extended kinematics. A computational modelling of extended continua is possible by a mixed finite element method. In this contribution, we show the introduction of internal rotational degrees of freedom to model also a stiffness with respect to roving flexure and twist. Furthermore, a corresponding structure-preserving time integration is obtained. Numerical examples also demonstrate the additional continuum stiffness owing to the consideration of roving flexure and twist.

1 INTRODUCTION

In rotordynamical systems, fiber-reinforced materials with fiber rovings and cured matrix material have gained great significance for engineers. For instance, there are woven roving structures as for turbine blades in Reference [3], or structures with unidirectional

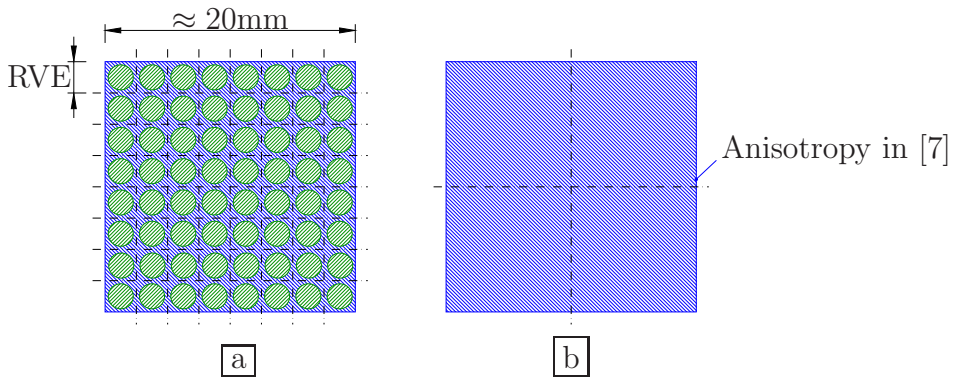

Figure 1: Sketch of the cross-section of a body with rovings [4] (diagram a). In [7], the stiffness effect of such rovings is modelled by anisotropy with *roving* tension and *curvature-twist stiffness* (diagram b).

rovings manufactured by the tailored fiber placement (TFP) for pump rotors in Reference [4]. Rovings are fiber bundles with a diameter in the range of millimeters (see Fig. 1), such that from a mechanical point of view a certain roving stiffness with respect to flexure and twist has to be taken into account. This is in contrast to the fabrication of fiber-reinforced materials by filaments, because here the fiber diameters are in the range of micrometers and a fiber flexure and twist stiffness can be neglected.

The computational modelling of fiber-reinforced materials based on filaments can be performed by an anisotropic Cauchy continuum based on structural tensors (see Reference [5]). The fibers are here assumed to be infinitely thin and only transmit tension forces along the fiber directions. But, as a finite diameter of rovings leads to a stiffness with respect to a local flexure and twist, the continuum formulation has to allow for length scales in the strain energy. Such length scales can be introduced by gradient-based continuum formulations as in Reference [6], or by continuum formulations with local rotational degrees of freedom as in Reference [7]. By means of the latter formulation, the flexure and twist can be associated with independent length scales, such that a flexural and a torsional rigidity can be prescribed independently as in structures.

Therefore, we follow Reference [7] and introduce by a mixed finite element method local rotational degrees of freedom, which are numerically independent, but physically connected to the displacement degrees of freedom due to the assumption of a perfect roving-matrix interface without slip. This local constraint is realized by a Hu-Washizu functional with respect to the antisymmetric part of the spatial velocity gradient of the continuum. Since we are interested in dynamic simulations in general, and in energy-momentum time integrations of dynamical problems in particular, we apply the mixed principle of virtual power in Reference [7] as rationale for transient finite element methods. Here, the space-time test functions fulfill the requirements of a Petrov-Galerkin method in time as in Reference [8], and simultaneously, the requirements of a discrete energy-momentum method in Reference [9] are satisfied for higher-order accuracies in time.

2 CONTINUUM MODEL AND ITS COMPUTATIONAL SETTING

We introduce local rotational degrees of freedom $\boldsymbol{\alpha} \in \mathbb{R}^{n_{\mathrm{dim}}}$ of a continuum body $\mathscr{B} \subset \mathbb{R}^{n_{\mathrm{dim}}}$ moving in the n_{dim}- dimensional Euclidean space by means of the identity

$$\mathbb{I}^{\mathrm{skw}} : \dot{\boldsymbol{F}}\boldsymbol{F}^{-1} = -\boldsymbol{\epsilon} \cdot \dot{\boldsymbol{\alpha}} \tag{1}$$

where $2\,\mathbb{I}^{\mathrm{skw}} = \boldsymbol{\epsilon} \cdot \boldsymbol{\epsilon}$ denotes the double skew-symmetric projection tensor expressed by the third-order Levi-Civita tensor $\boldsymbol{\epsilon}$. The second-order tensor $\boldsymbol{F} := \mathrm{Grad}[\boldsymbol{\varphi}]$ denotes the material gradient of the deformation $\boldsymbol{\varphi} : \mathscr{B}_0 \times [0,T] \to \mathscr{B}_t$ during the time interval $[0,T]$, that is the deformation gradient. We denote by $\mathscr{B}_0$ the initial configuration with position vectors $\boldsymbol{X} \in \mathscr{B}_0$, and $\mathscr{B}_t$ indicates the current configuration of the body $\mathscr{B}$ with position vectors $\boldsymbol{x} \in \mathscr{B}_t$. Thus, by means of the defined rotation mapping $\boldsymbol{\alpha} : \mathscr{B}_0 \times [0,T] \subset \mathbb{R}^{n_{\mathrm{dim}}} \times \mathbb{R} \to \mathbb{R}^{n_{\mathrm{dim}}}$, a local rotation (polar) vector $\boldsymbol{\gamma}(\boldsymbol{x}) \in \mathbb{R}^{n_{\mathrm{dim}}}$ at the material point $\boldsymbol{x} \in \mathscr{B}_t$ is defined. We enforce Eq. (1) by means of the Lagrange multiplier functional

$$\dot{I}\!I^{\mathrm{rot}}(\dot{\boldsymbol{\alpha}}, \dot{\boldsymbol{F}}, \boldsymbol{\tau}^t_{\mathrm{skw}}) := \int_{\mathscr{B}_0} \boldsymbol{\tau}^t_{\mathrm{skw}} : \boldsymbol{\epsilon} \cdot \left[\frac{1}{2}\, \boldsymbol{\epsilon} : \dot{\boldsymbol{F}}\boldsymbol{F}^{-1} + \dot{\boldsymbol{\alpha}} \right] \mathrm{d}V \tag{2}$$

using the Hu-Washizu method in the mixed principle of virtual power of Reference [7]. The Lagrange multiplier $\boldsymbol{\tau}^t_{\mathrm{skw}}$ denotes the skew-symmetric part of the Kirchhoff stress tensor. A variation with respect to the fields in the argument list leads to the corresponding equations or contributions of the time evolution equations. The variation $\delta_* \dot{\boldsymbol{F}}$ leads to the contribution of $\boldsymbol{\tau}^t_{\mathrm{skw}}$ in the equation of motion. The $*$ is a wildcard for 0 and 1, because we apply here zero-variations with respect to fields directly as in the principle of virtual work, and one-variations with respect to first time derivatives as in Jourdain's principle. Therefore, the designation 'mixed principle'. The $\delta_* \boldsymbol{\tau}^t_{\mathrm{skw}}$ variation leads to the weak form of Eq. (1). Finally, the $\delta_* \dot{\boldsymbol{\alpha}}$ variation furnishes a contribution of the independent local angular momentum balance equation. For more details see Reference [7].

2.1 Covariant formulation of the internal rotational degrees of freedom

In order to derive strain and stress measures associated with the internal rotational degrees of freedom, we start with a covariant formulation. Therefore, we consider curvilinear coordinates ξ^i, $i = 1, \ldots, n_{\mathrm{dim}}$, of a convected coordinate system (see Fig. 2). Analogous to the parametrization of the tangent vector $\mathrm{d}\boldsymbol{x}(\boldsymbol{\xi}, t)$, $\boldsymbol{\xi} = (\xi^1, \ldots, \xi^{n_{\mathrm{dim}}})$, by means of

$$\mathrm{d}\boldsymbol{x}(\boldsymbol{\xi}, t) = \frac{\partial \boldsymbol{x}(\boldsymbol{\xi}, t)}{\partial \xi^j}\, \mathrm{d}\xi^j \equiv \frac{\partial \boldsymbol{\varphi}(\boldsymbol{X}(\boldsymbol{\xi}), t)}{\partial \xi^j}\, \mathrm{d}\xi^j =: \mathrm{d}\xi^j\, \boldsymbol{g}_j \tag{3}$$

associated with the covariant basis vectors $\boldsymbol{g}_j$, $j = 1, \ldots, n_{\mathrm{dim}}$, we obtain $\mathrm{d}\boldsymbol{\gamma}(\boldsymbol{\xi}, t) = \mathrm{d}\alpha^k(\boldsymbol{\xi}, t)\, \boldsymbol{g}_k$ of the differential rotation vector $\mathrm{d}\boldsymbol{\gamma}(\boldsymbol{x}, t)$. By inserting the total differential $\mathrm{d}\alpha^k(\boldsymbol{\xi}, t) = \alpha^k_{,j}\, \mathrm{d}\xi^j$, we arrive at $\mathrm{d}\boldsymbol{\gamma} = \alpha^k_{,j}\, \mathrm{d}\xi^j\, \boldsymbol{g}_k =: \mathrm{d}\xi^j\, \boldsymbol{\gamma}_j$ with the vectors $\boldsymbol{\gamma}_j := \alpha^k_{,j}\, \boldsymbol{g}_k$ as

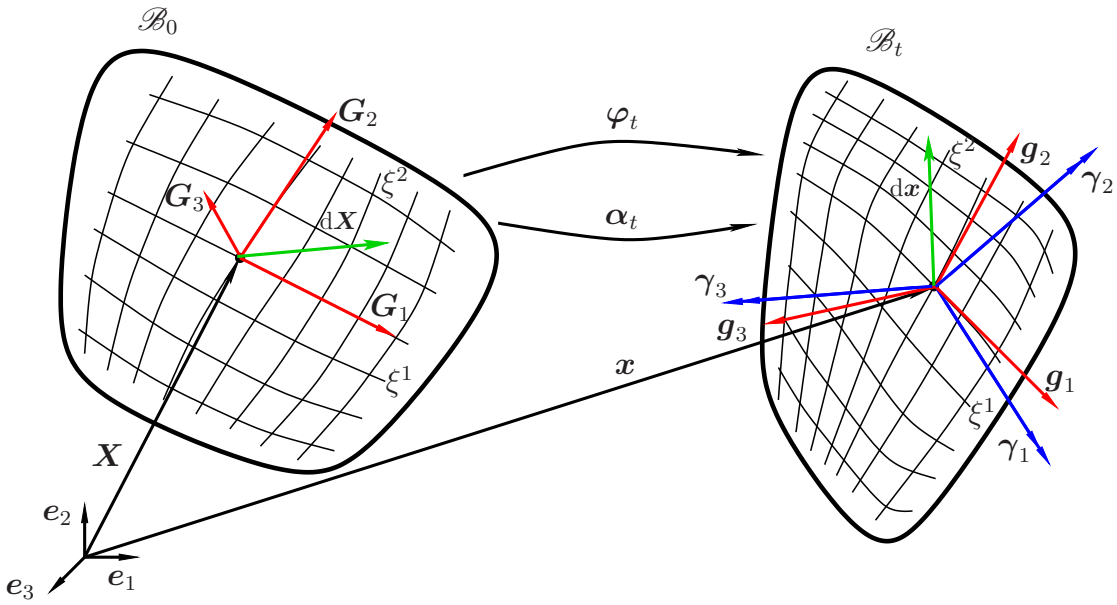

Figure 2: Initial configuration $\mathscr{B}_0$ and current configuration $\mathscr{B}_t$ with their covariant basis vectors $\boldsymbol{G}_i$ and $\boldsymbol{g}_i$, $i = 1,\dots,n_{\mathrm{dim}}$, respectively (red arrows) as well as the basis vectors $\boldsymbol{\gamma}_i := \alpha^k_{,i}\,\boldsymbol{g}_k$, (summation convention applied) pertaining to the local continuum rotation vector $\boldsymbol{\gamma}(\xi^1,\dots,\xi^{n_{\mathrm{dim}}},t) := \boldsymbol{\alpha}(\boldsymbol{X}(\xi^1,\dots,\xi^{n_{\mathrm{dim}}}),t)$ (blue double arrows) with the internal rotational degrees of freedom $\alpha^i(\xi^1,\dots,\xi^{n_{\mathrm{dim}}})$. Lines ξ^i denote curvilinear coordinates (cp. Reference [1]).

axial basis vectors. Hence, using the defined rotation mapping, the rotational covariant basis vectors can be analogously defined as

$$\boldsymbol{\gamma}_i := \frac{\partial \boldsymbol{\alpha}(\boldsymbol{X}(\boldsymbol{\xi}),t)}{\partial \xi^i} = \alpha^k_{,i}\,\boldsymbol{g}_k \tag{4}$$

Motivated by Reference [1], these covariant axial basis vectors are visualized in Fig. 2 by a double-arrow tripod. The rotational basis vectors $\boldsymbol{\gamma}_i$ directly lead to rotational metric coefficients $K_{ij} := \boldsymbol{g}_i \cdot \boldsymbol{\gamma}_j$ and $\gamma_{ij} := \boldsymbol{\gamma}_i \cdot \boldsymbol{\gamma}_j$. Whereas the coefficients K_{ij} define the covariant rotational basis vectors $\boldsymbol{\gamma}_j := K_{ij}\,\boldsymbol{g}^i$, the γ_{ij} define contravariant rotational basis vectors $\boldsymbol{\gamma}^i$. The metric coefficients K_{ij} define a rotational metric tensor denoted by

$$\boldsymbol{g}_\alpha := \frac{\partial \boldsymbol{\alpha}}{\partial \boldsymbol{x}} \equiv \mathrm{grad}[\boldsymbol{\alpha}] \tag{5}$$

where the operator grad[•] indicates the partial derivative with respect to $\boldsymbol{x} \in \mathscr{B}_t$. The rotation gradient $\boldsymbol{G}_\alpha := \mathrm{Grad}[\boldsymbol{\alpha}]$ maps the material tangent vector $\mathrm{d}\boldsymbol{X}$ into the differential rotation vector $\mathrm{d}\boldsymbol{\gamma}$. The curvature-twist tensor

$$\boxed{\boldsymbol{K} := \boldsymbol{F}^t\,\boldsymbol{g}_\alpha\,\boldsymbol{F}} \tag{6}$$

denotes a material deformation measure for differential vectors $\mathrm{d}\boldsymbol{x}$ with respect to the rotational metric tensor $\boldsymbol{g}_\alpha$. The superscript 't' indicates the tensor transposition.

2.2 Covariant formulation of transverse isotropy

We consider rovings embedded in a cured matrix material by assuming a perfect roving-matrix interface. We restrict us to one roving direction at each material point (transverse isotropy). We introduce a covariant kinematic formulation for the roving direction vector $\boldsymbol{a}_0$ in the initial configuration $\mathscr{B}_0$ and $\boldsymbol{a}_t$ in the current configuration $\mathscr{B}_t$, respectively. We first define the unstretched roving direction vector $\boldsymbol{a}_0 := a^i \boldsymbol{G}_i$ and the deformed roving direction vector $\boldsymbol{a}_t := a^i \boldsymbol{g}_i$ by using the covariant basis vectors. In this way, we obtain roving metric coefficients $G_F := \boldsymbol{a}_0 \cdot \boldsymbol{a}_0$ and $C_F := \boldsymbol{a}_t \cdot \boldsymbol{a}_t$, respectively. The metric coefficient C_F denotes the squared roving stretch. Note that, usually, the metric coefficient G_F is unity, but, formally, we are able to define contravariant roving direction vectors $\boldsymbol{a}_0^\flat := \boldsymbol{a}_0/G_F$ and $\boldsymbol{a}_t^\flat := \boldsymbol{a}_t/C_F$. The structural tensor $\boldsymbol{A}_0 := \boldsymbol{a}_0 \otimes \boldsymbol{a}_0^\flat$ plays the role of an identity tensor. The roving deformation gradient $\boldsymbol{F}_F := \boldsymbol{a}_t \otimes \boldsymbol{a}_0^\flat$ maps the initial roving direction vector $\boldsymbol{a}_0$ to the current roving vector $\boldsymbol{a}_t$. Analogous to the deformation of line elements $\mathrm{d}\boldsymbol{x}$, derived by using the inner product $\langle \mathrm{d}\boldsymbol{x}, \mathrm{d}\boldsymbol{x} \rangle_{\boldsymbol{g}}$ with respect to the translational metric tensor $\boldsymbol{g}$, we derive the roving deformation by using the inner product $\langle \boldsymbol{a}_t, \mathrm{d}\boldsymbol{x} \rangle_{\boldsymbol{g}}$. Accordingly, we arrive at the roving deformation tensor

$$\boldsymbol{C}_A := \boldsymbol{F}_F^t \, \boldsymbol{g} \, \boldsymbol{F} \equiv \boldsymbol{A}_0 \, \boldsymbol{C} \tag{7}$$

where $\boldsymbol{C} := \boldsymbol{F}^t \, \boldsymbol{g} \, \boldsymbol{F}$ denotes the right Cauchy-Green tensor of the body. The basic invariants $I_4(\boldsymbol{C}, \boldsymbol{a}_0) := \boldsymbol{a}_0 \cdot \boldsymbol{C} \cdot \boldsymbol{a}_0 \equiv C_F$ and $J_5(\boldsymbol{C}, \boldsymbol{a}_0) := \boldsymbol{a}_0 \cdot \boldsymbol{C}\boldsymbol{C} \cdot \boldsymbol{a}_0$, which measure the squared roving stretch C_F and the distorsion of the rovings with respect to the matrix material, respectively, can be then replaced by

$$I_1(\boldsymbol{C}_A) := \boldsymbol{C}_A : \boldsymbol{G}^{-1} = \frac{I_4(\boldsymbol{C}, \boldsymbol{a}_0)}{G_F} \qquad J_2(\boldsymbol{C}_A) := \boldsymbol{C}_A : \boldsymbol{C}_A = \frac{J_5(\boldsymbol{C}, \boldsymbol{a}_0)}{G_F} \tag{8}$$

with the translational metric tensor $\boldsymbol{G}$ with respect to the reference configuration $\mathscr{B}_0$. The roving curvature-twist deformation can be analogously determined by the inner product $\langle \boldsymbol{a}_t, \mathrm{d}\boldsymbol{x} \rangle_{\boldsymbol{g}_\alpha}$ with respect to the rotational metric tensor $\boldsymbol{g}_\alpha$. This leads to the tensor

$$\boxed{\boldsymbol{K}_F := \boldsymbol{F}_F^t \, \boldsymbol{g}_\alpha \, \boldsymbol{F} \equiv \boldsymbol{A}_0 \, \boldsymbol{K}} \tag{9}$$

as roving curvature-twist tensor. The basic invariants

$$I_1(\boldsymbol{K}_F) := \boldsymbol{K}_F : \boldsymbol{G}^{-1} = \frac{T_F}{G_F} \qquad J_2(\boldsymbol{K}_F) := \boldsymbol{K}_F : \boldsymbol{K}_F = \frac{1}{2} \frac{B_F}{G_F} \tag{10}$$

measure the roving twist T_F per unit length G_F and the curvature B_F of rovings with unit length G_F, respectively. We also aim at the consideration of rovings with organic fibers, which are viscoelastic and thus described by an 'intermediate roving configuration'. In Tab. 1, we therefore summarize the complete formulation by using the notation of the covariant formulation of transverse isotropy.

Table 1: Kinematics of *viscoelastic* rovings (transverse isotropy) for perfect roving-matrix interface.

	Covariant roving basis vector	Contravariant roving basis vector
(T.1.1)	$\bar{\boldsymbol{a}} \cdot \bar{\boldsymbol{a}} =: C_F^v$	$\bar{\boldsymbol{a}}^\flat = \frac{1}{C_F^v}\,\bar{\boldsymbol{a}} \quad \bar{\boldsymbol{a}}^\flat \cdot \bar{\boldsymbol{a}} = 1$
	Roving metric tensor (structural tensor)	Roving right Cauchy-Green tensor
(T.1.2)	$\bar{\boldsymbol{a}} = \bar{\boldsymbol{A}}\,\bar{\boldsymbol{a}} \quad \bar{\boldsymbol{A}} = \bar{\boldsymbol{a}} \otimes \bar{\boldsymbol{a}}^\flat$	$\boldsymbol{C}_F := \boldsymbol{F}_F^t\,\boldsymbol{F}_F = C_F\,\boldsymbol{a}_0^\flat \otimes \boldsymbol{a}_0^\flat$
	Roving deformation gradients	Inverse roving deformation gradients
(T.1.3)	$\bar{\boldsymbol{a}} = \boldsymbol{F}_F^v\,\boldsymbol{a}_0 \quad \boldsymbol{F}_F^v := \bar{\boldsymbol{a}} \otimes \boldsymbol{a}_0^\flat$ $\boldsymbol{a}_t = \boldsymbol{F}_F^e\,\bar{\boldsymbol{a}} \quad \boldsymbol{F}_F^e := \boldsymbol{a}_t \otimes \bar{\boldsymbol{a}}^\flat$	$\boldsymbol{f}_F^v\,\boldsymbol{F}_F^v = \boldsymbol{A}_0 \quad \boldsymbol{f}_F^v := \boldsymbol{a}_0 \otimes \bar{\boldsymbol{a}}^\flat \quad \boldsymbol{F}_F^v\,\boldsymbol{f}_F^v = \bar{\boldsymbol{A}}$ $\boldsymbol{f}_F^e\,\boldsymbol{F}_F^e = \bar{\boldsymbol{A}} \quad \boldsymbol{f}_F^e := \bar{\boldsymbol{a}} \otimes \boldsymbol{a}_t^\flat \quad \boldsymbol{F}_F^e\,\boldsymbol{f}_F^e = \boldsymbol{g}_F$
	Roving push forward	Roving pull back
(T.1.4)	$\bar{\boldsymbol{a}} = \boldsymbol{F}_F^v \cdot \boldsymbol{a}_0 \quad \bar{\boldsymbol{a}}^\flat = [\boldsymbol{f}_F^v]^t\,\boldsymbol{a}_0^\flat$ $\boldsymbol{a}_t = \boldsymbol{F}_F^e \cdot \bar{\boldsymbol{a}} \quad \boldsymbol{a}_t^\flat = [\boldsymbol{f}_F^e]^t\,\bar{\boldsymbol{a}}^\flat$	$\boldsymbol{a}_0 = \boldsymbol{f}_F^v \cdot \bar{\boldsymbol{a}} \quad \boldsymbol{a}_0^\flat = [\boldsymbol{F}_F^v]^t\,\bar{\boldsymbol{a}}^\flat$ $\bar{\boldsymbol{a}} = \boldsymbol{f}_F^e \cdot \boldsymbol{a}_t \quad \bar{\boldsymbol{a}}^\flat = [\boldsymbol{F}_F^e]^t\,\boldsymbol{a}_t^\flat$
	Viscous roving deformation tensor	Elastic roving deformation tensor
(T.1.5)	$\bar{\boldsymbol{a}} \cdot \bar{\boldsymbol{a}} = \boldsymbol{a}_0 \cdot [\boldsymbol{F}_F^v]^t \boldsymbol{F}_F^v \cdot \boldsymbol{a}_0 =: \boldsymbol{a}_0 \cdot \boldsymbol{C}_F^v \cdot \boldsymbol{a}_0$ $\boldsymbol{C}_F^v := C_F^v\,\boldsymbol{a}_0^\flat \otimes \boldsymbol{a}_0^\flat$	$\boldsymbol{a}_t \cdot \boldsymbol{a}_t = \bar{\boldsymbol{a}} \cdot [\boldsymbol{F}_F^e]^t \boldsymbol{F}_F^e \cdot \bar{\boldsymbol{a}} =: \bar{\boldsymbol{a}} \cdot \boldsymbol{C}_F^e \cdot \bar{\boldsymbol{a}}$ $\boldsymbol{C}_F^e := C_F\,\bar{\boldsymbol{a}}^\flat \otimes \bar{\boldsymbol{a}}^\flat$
	Inverse viscous roving deformation tensor	Inverse elastic roving deformation tensor
(T.1.6)	$[\boldsymbol{C}_F^v]^{-1}\boldsymbol{C}_F^v = \boldsymbol{A}_0 \quad [\boldsymbol{C}_F^v]^{-1} := \frac{1}{C_F^v}\,\boldsymbol{a}_0 \otimes \boldsymbol{a}_0$	$[\boldsymbol{C}_F^e]^{-1}\boldsymbol{C}_F^e = \bar{\boldsymbol{A}} \quad [\boldsymbol{C}_F^e]^{-1} := \frac{1}{C_F}\,\bar{\boldsymbol{a}} \otimes \bar{\boldsymbol{a}}$
	Viscous roving invariant	Elastic roving invariant
(T.1.7)	$I_1(\boldsymbol{C}_F^v) := \boldsymbol{C}_F^v : \boldsymbol{A}_0 \equiv \frac{C_F^v}{G_F}$	$I_1(\boldsymbol{C}_F^e) := \boldsymbol{C}_F^e : \bar{\boldsymbol{A}} \equiv \boldsymbol{C}_F\,[\boldsymbol{C}_F^v]^{-1} : \boldsymbol{A}_0 = \frac{C_F}{C_F^v}$

2.3 Power-conjugated strain and stress tensors for rotational deformations

In Reference [7], the weak formulation is derived by using power-conjugated strain and stress tensors. Therefore, we here define rotational strain rate tensors. We obtain the rotation velocity gradient $\dot{\boldsymbol{G}}_\alpha := \dot{\boldsymbol{\gamma}}_i \otimes \boldsymbol{G}^i$ which maps the tangent vector $\mathrm{d}\boldsymbol{X}$ into the differential rate vector $\mathrm{d}\dot{\boldsymbol{\gamma}}$. A material rotation velocity gradient and a spatial rotation velocity gradient, respectively, are then defined by

$$\boldsymbol{L}_\alpha := \boldsymbol{G}_\alpha^{-1}\,\dot{\boldsymbol{G}}_\alpha \qquad\qquad \boldsymbol{l}_\alpha := \dot{\boldsymbol{G}}_\alpha\,\boldsymbol{G}_\alpha^{-1} \tag{11}$$

respectively. We arrive at a material curvature-twist rate tensor $\boldsymbol{D}_\alpha := \boldsymbol{L}^t\,\boldsymbol{K} + \boldsymbol{K}\,\boldsymbol{L}_\alpha$ with the inner product $\langle \mathrm{d}\boldsymbol{x}, \mathrm{d}\boldsymbol{x} \rangle_{\boldsymbol{g}_\alpha}$ by means of

$$\overset{\cdot}{\mathrm{d}\boldsymbol{x} \cdot \mathrm{d}\boldsymbol{\gamma}} = \mathrm{d}\boldsymbol{X} \cdot \dot{\boldsymbol{K}} \cdot \mathrm{d}\boldsymbol{X} =: \mathrm{d}\boldsymbol{X} \cdot \boldsymbol{D}_\alpha \cdot \mathrm{d}\boldsymbol{X} \tag{12}$$

The corresponding spatial curvature-twist rate tensor is defined as the Lie-derivative

$$\boldsymbol{d}_\alpha := \left(\boldsymbol{l}^t + \boldsymbol{l}_\alpha\right) \boldsymbol{g}_\alpha = \overset{\square}{\boldsymbol{g}}_\alpha := \dot{K}_{ij}\,\boldsymbol{g}^i \otimes \boldsymbol{g}^j \tag{13}$$

As next step, we derive the power-conjugated stress tensors. In view of the meaning of the curvature-twist tensor $\boldsymbol{K}$ or the rotational metric tensor $\boldsymbol{g}_\alpha$, respectively, we assume a general rotational strain energy function $\Psi_K(\boldsymbol{K})$, in analogy to an hyperelastic strain energy function $\Psi_M(\boldsymbol{C})$. After differentiating the rotational strain energy function $\Psi_K(\boldsymbol{K})$ with respect to time, we obtain the curvature-twist stress tensor

$$\boldsymbol{S}_K := \frac{\partial \Psi_K}{\partial \boldsymbol{K}} \tag{14}$$

which is power-conjugated to the material curvature-twist rate tensor $\boldsymbol{D}_\alpha = \dot{\boldsymbol{K}}$. Bearing in mind the definition of the curvature-twist tensor in Eq. (6), we arrive at the tensors

$$\boldsymbol{N}_K := \boldsymbol{G}_\alpha \, \boldsymbol{S}_K^t \qquad\qquad \boldsymbol{P}_K := \boldsymbol{F} \, \boldsymbol{S}_K \tag{15}$$

to which we refer to as Piola-Kirchhoff curvature-twist stress tensor and Piola-Kirchhoff couple stress tensor due to their power-conjugated relation to $\boldsymbol{L} := \boldsymbol{F}^{-1} \, \dot{\boldsymbol{F}}$ and $\boldsymbol{L}_\alpha$, respectively. Note that the Piola-Kirchhoff couple stress tensor $\boldsymbol{P}_K$ possesses the same tensorial basis as the first Piola-Kirchhoff stress tensor $\boldsymbol{P}$. Finally, we take into account that the spatial curvature-twist rate tensor in Eq. (13) represents the push forward of the material curvature-twist rate tensor $\dot{\boldsymbol{K}}$. Therefore, we arrive at the 'spatial tensors'

$$\boldsymbol{\tau}_K^t := \boldsymbol{F} \, \boldsymbol{N}_K^t \equiv \boldsymbol{F} \, \boldsymbol{S}_K \, \boldsymbol{G}_\alpha^t \qquad\qquad \boldsymbol{\mu}_K := \boldsymbol{P}_K \, \boldsymbol{F}^t \equiv \boldsymbol{F} \, \boldsymbol{S}_K \, \boldsymbol{F}^t \tag{16}$$

Owing to the analogy with the well-known Kirchhoff stress tensor $\boldsymbol{\tau}$, we refer to $\boldsymbol{\tau}_K^t$ as Kirchhoff curvature-twist stress tensor and to $\boldsymbol{\mu}_K$ as Kirchhoff couple stress tensor. Analogous to the Piola-Kirchhoff stress tensor $\boldsymbol{\tau}$, the Kirchhoff couple stress tensor $\boldsymbol{\mu}_K$ is defined with respect to the spatial basis vectors $\boldsymbol{g}_i$, $i = 1, \ldots, n_{\text{dim}}$.

2.4 The algorithmic stress tensor for rotational strain energy functions

An energy-consistent stress approximation can be derived as an extension of an objective stress tensor, which corrects the error in the gradient theorem of the strain energy function. In Reference [10], a material stress tensor is considered, but in Reference [11] is motivated, that the extension of a spatial stress tensor, and a subsequent pull back, is more appropriate from a continuum mechanical point of view. We follow the latter design procedure and extend an appropriate spatial rotational stress tensor. Thereby, we assume the existence of an elastic strain energy function $\Psi_K(\boldsymbol{K})$ for the rotational stress tensors. An algorithmic stress tensor $\bar{\boldsymbol{S}}_K$ for an energy-momentum scheme ensures the satisfaction of the internal potential energy balance by fulfilling the local equation

$$\Psi_K(\boldsymbol{K}(\boldsymbol{X}, t_{n+1})) - \Psi_K(\boldsymbol{K}(\boldsymbol{X}, t_n)) = \int_{t_n}^{t_{n+1}} \dot{\Psi}_K(\boldsymbol{K}(\boldsymbol{X}, t)) \, \mathrm{d}t \equiv \int_0^1 \overset{\circ}{\overline{\Psi_K}} \, (\boldsymbol{K}(\boldsymbol{X}, \alpha)) \, \mathrm{d}\alpha \tag{17}$$

with $\alpha(t) := (t - t_n)/(t_{n+1} - t_n)$ for any function $\Psi_K(\boldsymbol{K})$ on each time step $[t_n, t_{n+1}]$ or normalized time interval $[0, 1]$, respectively. We denote by a superimposed $\circ$ the derivative

with respect to the normalized time $\alpha \in [0,1]$. The stress tensor $\bar{\boldsymbol{S}}_K(\alpha)$ is determined by means of a constrained variational problem associated with the Lagrange functional

$$\mathcal{F}_K(\bar{\boldsymbol{S}}_K, \lambda_K) := \lambda_K \, \mathcal{G}_K(\bar{\boldsymbol{S}}_K) + \int_0^1 F_K(\bar{\boldsymbol{S}}_K(\alpha)) \, \mathrm{d}\alpha \tag{18}$$

where the dependencies on $\boldsymbol{X} \in \mathscr{B}_0$ have been omitted. The scalar-valued and time-independent Lagrange multiplier λ_K enforces the constraint

$$\mathcal{G}_K(\bar{\boldsymbol{S}}_K) := \Psi_K(\boldsymbol{K}(t_{n+1})) - \Psi_K(\boldsymbol{K}(t_n)) - \int_0^1 G_K(\bar{\boldsymbol{S}}_K(\alpha)) \, \mathrm{d}\alpha \tag{19}$$

with

$$G_K(\bar{\boldsymbol{S}}_K) := \left[\bar{\boldsymbol{S}}_K + \frac{\partial \Psi_K(\boldsymbol{K})}{\partial \boldsymbol{K}} \right] : \overset{\circ}{\boldsymbol{K}}(\alpha) \tag{20}$$

A crucial aspect is the choice of the least-squares function $F_K(\bar{\boldsymbol{S}}_K)$. Here, we find different possibilities [10, 11]. In the latter reference, the algorithmic stress is based on a least-squares function with respect to a spatial stress measure in order to simulate with an optimal 'true stress'. We follow this approach and consider

$$F_K := \frac{1}{2} \, \bar{\mu}^{ij} \, \boldsymbol{g}_i \otimes \boldsymbol{g}_j : \bar{\mu}^{kl} \, \boldsymbol{g}_k \otimes \boldsymbol{g}_l = \frac{1}{2} \, g_{ki} \, \bar{\mu}^{ij} \, \bar{\mu}^{kl} \, g_{lj} = \frac{1}{2} \, \boldsymbol{g} \, \bar{\boldsymbol{\mu}} : \bar{\boldsymbol{\mu}} \, \boldsymbol{g} \tag{21}$$

where $\bar{\boldsymbol{\mu}}$ denotes an algorithmic Kirchhoff couple stress tensor, which is related by a pull back operation with the actual algorithmic stress tensor $\bar{\boldsymbol{S}}_K$. Therefore, we arrive at

$$F_K(\bar{\boldsymbol{S}}_K) := \frac{1}{2} \, \boldsymbol{g} \cdot \boldsymbol{F} \, \bar{\boldsymbol{S}}_K \, \boldsymbol{F}^t : \boldsymbol{F} \, \bar{\boldsymbol{S}}_K \, \boldsymbol{F}^t \cdot \boldsymbol{g} = \frac{1}{2} \, \boldsymbol{C} \, \bar{\boldsymbol{S}}_K : \bar{\boldsymbol{S}}_K \, \boldsymbol{C} \tag{22}$$

In contrast, Reference [11] reveals that the least-squares function corresponding to the strain energy $\Psi_M(\boldsymbol{C})$ is associated with an algorithmic Kirchhoff stress tensor $\bar{\boldsymbol{\tau}}$. The important similarity to this work is the identical tensorial basis of $\bar{\boldsymbol{\mu}}$ and $\bar{\boldsymbol{\tau}}$. The next step is the functional minimization of the Lagrange functional in Eq. (18). The minimization condition is given by the vanishing variational form

$$\delta_* \mathcal{F}_K(\bar{\boldsymbol{S}}_K, \lambda_K) \equiv \int_0^1 \boldsymbol{C} \, \bar{\boldsymbol{S}}_K \, \boldsymbol{C} : \delta_* \bar{\boldsymbol{S}}_K \, \mathrm{d}\alpha - \lambda_K \int_0^1 \overset{\circ}{\boldsymbol{K}} : \delta_* \bar{\boldsymbol{S}}_K \, \mathrm{d}\alpha + \delta_* \lambda_K \, \mathcal{G}_K(\bar{\boldsymbol{S}}_K) = 0 \tag{23}$$

which leads to the Euler-Lagrange equations

$$\boldsymbol{C} \, \bar{\boldsymbol{S}}_K \, \boldsymbol{C} = \lambda_K \, \overset{\circ}{\boldsymbol{K}} \qquad\qquad \mathcal{G}_K(\bar{\boldsymbol{S}}_K) = 0 \tag{24}$$

The functional operator δ_* also indicates a variation with respect to each field in the argument list of a functional, here $\mathcal{F}_K(\bar{\boldsymbol{S}}_K, \lambda_K)$. We combine Eqs. (24) and arrive at the

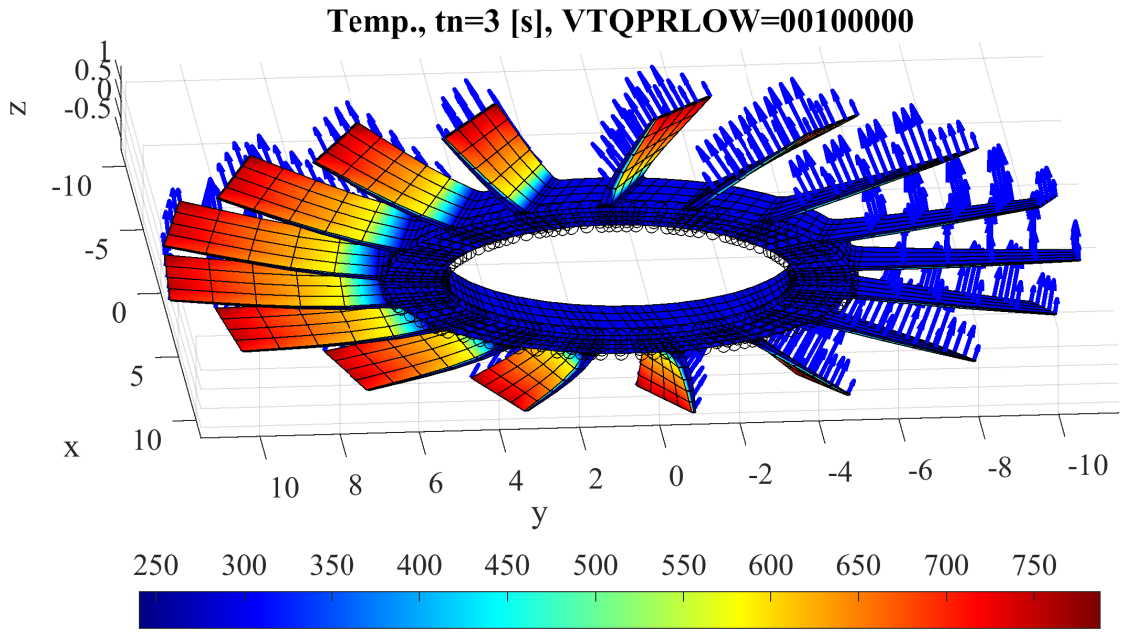

Figure 3: Fiber-reinforced pump rotor with $n_{\text{el}} = 2584$ hexahedron elements H8 and 'D1G1V0F0 H8' space approximation: Current configuration at time $t_n = 3.0$. The colors indicate the current temperature. Blue arrows denote the applied boundary heat flux $\bar{Q}^A$ (Vector information VTQPRLOW=00100000). A high heat conduction and temperature Dirichlet boundaries lead to a cool rotor.

tensor $\bar{\boldsymbol{S}}_K = \lambda_K \boldsymbol{C}^{-1} \overset{\circ}{\boldsymbol{K}} \boldsymbol{C}^{-1}$ with

$$\lambda_K = \frac{\Psi_K(\boldsymbol{K}(t_{n+1})) - \Psi_K(\boldsymbol{K}(t_n)) - \int_0^1 \frac{\partial \Psi_K(\boldsymbol{K})}{\partial \boldsymbol{K}} : \overset{\circ}{\boldsymbol{K}}(\alpha)\, \mathrm{d}\alpha}{\int_0^1 \boldsymbol{C}^{-1} \overset{\circ}{\boldsymbol{K}}(\alpha) : \overset{\circ}{\boldsymbol{K}}(\alpha)\, \boldsymbol{C}^{-1}\, \mathrm{d}\alpha} \tag{25}$$

This algorithmic stress tensor $\bar{\boldsymbol{S}}_K$ satisfies the gradient theorem in Eq. (17) for any time step size $h_n := t_{n+1} - t_n$, so that the weak formulation in Reference [7] extended by Eq. (25) furthermore satisfies each balance law in Reference [7].

3 NUMERICAL EXAMPLE

We show now the algorithmic energy-momentum consistency of $\bar{\boldsymbol{S}}_K$ by a simulation with the 121-em-scheme in Reference [7]. This energy-momentum scheme is based on linear finite elements in time for mechanical state variables, quadratic finite elements in time for temperature and entropy and also linear finite elements in time for viscous time evolution variables. The used special mixed finite element formulation is called 'D1G1V0F0 H8' method, and consists of (i) tri-linear eight-noded hexahedron (H8) elements for the deformation and rotation mapping (D1), (ii) extended linear tetrahedron (T4+) elements for independent gradient fields (G1), and (iii) one-noded tetrahedron (T1) elements for

independent volumetric strains (V0) and roving strains (F0). In the plot of the current configuration in Fig. 3, we also provide vector fields by colored arrows denoted by 'VTQPRLOW'. The label 'V' indicates the velocity field, 'T' denotes Neumann traction loads, 'Q' designates Neumann heat fluxes, 'P' pressure follower loads, 'R' denotes Dirichlet reaction forces, 'L' the Dirichlet heat fluxes, 'O' indicates the angular velocity field and 'W' the torque vector field. We consider the pump rotor in Reference [4]. Each blade of the rotor consists of a double-layered laminate. The directions of the rovings in each blade are tangential to the surface of the blade and 'crossed' to each other. In the hub and the chamfer, we assume rovings in tangential direction. The motion is completely initiated by applied mechanical loads. The rotation mainly arises from the anti-clockwise torque load $\bar{W}_z^A = -\hat{W}_z\, f(t)$ parallel to the z-axis in boundary nodes on the top of the hub (see the definition of $f(t)$ in Reference [7]). But, we also load the front of the blades with a pressure follower load $f_p(t) := \hat{p}\,|\sin(\omega_{\text{load,p}}\, t)|$. As thermal Neumann load, we introduce on the front of the blades an inward transient heat flux $\bar{Q}^A = \hat{Q}\, f(t)$. On the back of the blades and the bottom as well as the inner side of the hub, we prescribe a constant ambient temperature Θ_∞.

Fig. 4 demonstrates the energy-momentum consistency of $\bar{\boldsymbol{S}}_K$ by means of the errors of the mechanical balance laws. Intra-processing balances represent convergence criteria and are thus determined within the iteration loop. Post-processing balances are calculated after terminating the global Newton-Raphson procedure by taking into account generalized reactions. The balance laws are therefore satisfied for each implemented boundary condition. In the upper left plot, we show that the potential energy balance is fulfilled. The axes are normalized by the prescribed Newton-Raphson tolerance TOL. In the right column of Fig. 4, we show the fulfilled linear and angular momentum balances. The angular momentum balance includes the spin angular momentum associated with the internal rotational degrees of freedom.

4 CONCLUSIONS

An extended continuum formulation is derived by a mixed finite element formulation which introduces internal rotational degrees of freedom by the Hu-Washizu method. In this way, a local rotational stiffness is introduced by an additional strain energy function. This formulation allows the material modelling of fiber-reinforced materials based on rovings. An algorithmic stress tensor in the sense of References [10, 11] demands a detailed specification of the corresponding kinematic formulation. Therefore, we start with a covariant formulation with respect to curvilinear coordinates. In this way, we show that the internal rotational degrees of freedom are associated with a metric tensor for rotational deformations. The summarized numerical example demonstrates the algorithmic energy-momentum consistency of the new couple stress approximation.

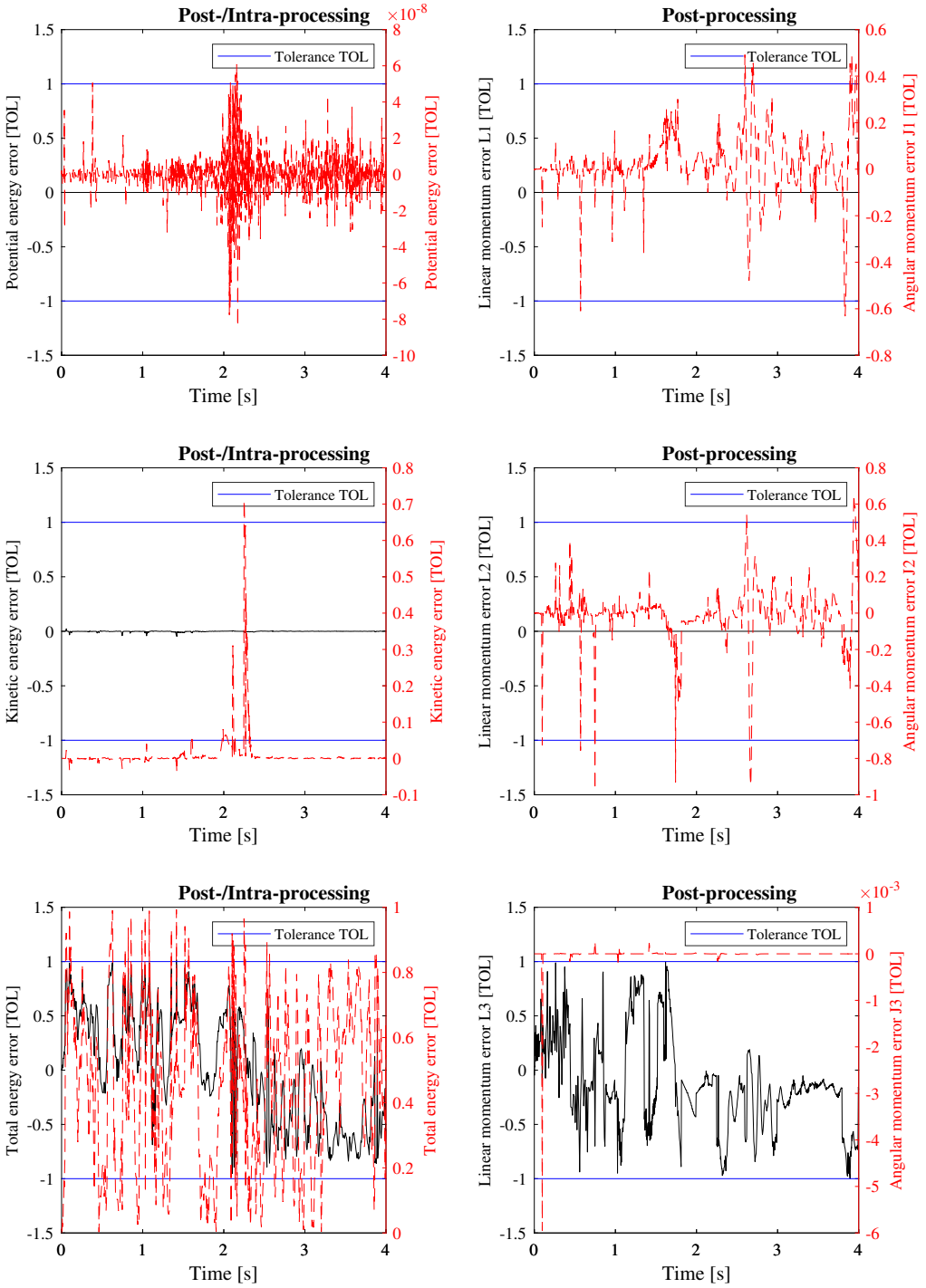

Figure 4: Fiber-reinforced pump rotor with $n_{\text{el}} = 2584$ hexahedron elements H8 and 'D1G1V0F0 H8' space approximation: Error of mechanical balance laws in the time interval [0 4.0].

Acknowledgements This work is provided by the 'Deutsche Forschungsgemeinschaft' under the grants GR 3297/4-2 and GR 3297/6-1. This support is gratefully acknowledged.

REFERENCES

[1] Wriggers P. Nonlinear finite element methods, Springer, (2008).

[2] Wriggers P. The Art of Modeling in Solid Mechanics. In *The Art of Modeling Mechanical Systems*, p. 321–386, Springer, (2017).

[3] De Luycker E. and Morestin F. and Boisse P. and Marsal D. Simulation of 3D interlock composite preforming. *Composite Structures* (2009) **88**(4):615–623.

[4] Uhlig K. *Beitrag zur Anwendung der Tailored Fiber Placement Technologie am Beispiel von Rotoren aus kohlenstofffaserverstärktem Epoxidharz für den Einsatz in Turbomolekularpumpen*, Doctoral thesis, Technische Universität Dresden, (2018), urn:nbn:de:bsz:14-qucosa-235151.

[5] Reese S. and Raible T. and Wriggers P. Finite element modelling of orthotropic material behaviour in pneumatic membranes. *International journal of solids and structures* (2001) **38**(52):9525–9544.

[6] Asmanoglo T. and Menzel A. A multi-field finite element approach for the modelling of fibre-reinforced composites with fibre-bending stiffness. *Comput. Methods Appl. Mech. Engrg.* (2017) **317**:1037–1067.

[7] Groß M., Dietzsch J. and Röbiger C. Non-isothermal energy–momentum time integrations with drilling degrees of freedom of composites with viscoelastic fiber bundles and curvature–twist stiffness continua. *Comput. Methods Appl. Mech. Engrg.* (2020) **365**:112973.

[8] Betsch P. and Steinmann P. Conservation properties of a time FE method—part II: Time-stepping schemes for non-linear elastodynamics. *Int. J. Numer. Methods Engng.* (2001) **50**(8):1931–1955.

[9] Simo J.C. and Tarnow N. The Discrete Energy-Momentum Method. Conserving Algorithms for Nonlinear Elastodynamics. *Z. angew. Math. Phys.* (1992) **43**:757–792.

[10] Gonzalez O. *Design and analysis of conserving integrators for nonlinear Hamiltonian systems with symmetry.* Stanford University, Stanford, CA, USA, (1996).

[11] Armero F. and Zambrana-Rojas C. Volume-preserving energy–momentum schemes for isochoric multiplicative plasticity. *Comput. Methods Appl. Mech. Engrg.* (2007) **196**:4130–4159.